International Journal of Applied Earth Observation and Geoinformation 120 (2023) 103347

Contents lists available at ScienceDirect

International Journal of Applied Earth Observation and Geoinformation

journal homepage: www.elsevier.com/locate/jag

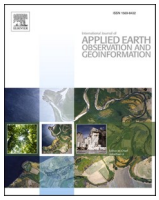

Assessment of gridded datasets of various near surface temperature variables over Heihe River Basin: Uncertainties, spatial heterogeneity and clear-sky bias

Shuo Xu [a], Dongdong Wang [a,*], Shunlin Liang [b], Yuling Liu [c], Aolin Jia [a]

[a] Department of Geographical Sciences, University of Maryland, College Park, MD 20742, USA
[b] Department of Geography, University of Hong Kong, 999077, Hong Kong, China
[c] Earth System Science Interdisciplinary Center, University of Maryland, College Park, MD 20740, USA

ARTICLE INFO

Keywords:
Temperature
Near surface temperature
Land surface temperature
Air temperature
Soil temperature
Validation
Spatial heterogeneity
Clear-sky bias

ABSTRACT

Near-surface temperatures, such as air, land surface, and soil temperatures, play significant roles in surface radiation and energy balance. This study assessed nine gridded near-surface temperature products and analyzed the spatial heterogeneity and clear-sky bias of these temperature variables, using extensive measurements collected at Heihe River Basin. The MXD21 (MOD21 and MYD21) product had the lowest root mean square error (RMSE) (3.35 K) among all skin temperature products but a high percentage of missing values (48.4 %). All-weather skin temperature products had comparable accuracy for the interpolated cloudy-sky cases (RMSE 4.92 K) and observed clear-sky pixels (RMSE 3.42 K). For air temperature, AMSR2 had the lowest RMSE (2.48 K), but a high percentage of invalid data (32.5 %); and ERA5 had a worse accuracy (RMSE 3.87 K) but a high spatial resolution and gap-free data coverage. Comparing products from the same data source, air and soil temperatures had higher accuracies than skin temperature. Among the different variables of temperature, the 0 cm soil temperature and skin temperature had higher spatiotemporal heterogeneity than the air temperature and the soil temperatures at greater depths. The skin temperature, 0 cm soil temperature, and air temperature had higher clear-sky biases compared to soil temperatures.

1. Introduction

Near-surface temperatures are vital climate variables that play a significant role in physical and biological processes in the atmosphere, biosphere, and hydrosphere (Benali et al. 2012; Jia et al. 2023; Muro et al. 2018). These variables can be measured at different levels and have different physical interpretations and scientific applications. Air temperature is a fundamental indicator of surface environmental conditions (Jia et al. 2020) and a direct indicator of global warming (Zhang et al. 2021), and it has a long history of observational data records (Nieto et al. 2011). Skin temperature, also known as land surface temperature (LST) or sea surface temperature (SST) (Sobrino et al. 2020), is directly related to the radiative process at the surface that determines the upward longwave radiation emitting from the Earth's surface (Li et al. 2013b; Xu et al. 2021). Soil temperature is a key parameter of soil physical conditions that affects plant root growth, physiological activity, and the hydrothermal regime in permafrost regions (Yang et al. 2020). It also indicates anomalies at the land surface and affects heat exchange between the land surface and atmosphere (Hu and Feng 2004). These temperature variables are traditionally measured at field stations, and the measurements have high accuracy and temporal resolution (Vancutsem et al. 2010); however, such measurements have limited spatial coverage due to sparsely distributed sites.

Satellite remote sensing is advantageous in providing high-density spatial sampling over large areas (Li et al. 2013b). It offers various types of near-surface temperature products, including thermal infrared (TIR), passive microwave (PMW), re-analysis, and all-weather temperature products. Different in-situ data and validation methods are used by many authors to validate these temperature products, and they typically focus on a single temperature product (Cao et al. 2020; Duan et al. 2019; Duan et al. 2018; Gleixner et al. 2020; Jones et al. 2010; Trigo and Macedo 2015; Xu and Cheng 2021; Zhang 2017; Zhang et al. 2019). However, comparing the validation results of different temperature products is challenging due to differences in in-situ data and validation

* Corresponding author.
E-mail address: ddwang@umd.edu (D. Wang).

https://doi.org/10.1016/j.jag.2023.103347
Received 12 December 2022; Received in revised form 3 May 2023; Accepted 6 May 2023
Available online 12 May 2023

Table 1
Key information for the temperature datasets used in this study.

Name in this study	Short name	Product name	Variables	Product type	Spatial resolution	Temporal resolution
MXD11	**MOD11A1**	MODIS/Terra Land Surface Temperature/Emissivity Daily L3 Global 1 km SIN Grid V061	Skin temperature	TIR	1 km	Daily
	MYD11A1	MODIS/Aqua Land Surface Temperature/Emissivity Daily L3 Global 1 km SIN Grid V061	Skin temperature	TIR	1 km	Daily
MXD21	**MOD21A1D**	MODIS/Terra Land Surface Temperature/3-Band Emissivity Daily L3 Global 1 km SIN Grid Day V061	Skin temperature	TIR	1 km	Daily
	MYD21A1D	MODIS/Aqua Land Surface Temperature/3-Band Emissivity Daily L3 Global 1 km SIN Grid Day V061	Skin temperature	TIR	1 km	Daily
	MOD21A1N	MODIS/Terra Land Surface Temperature/3-Band Emissivity Daily L3 Global 1 km SIN Grid Night V061	Skin temperature	TIR	1 km	Daily
	MYD21A1N	MODIS/Aqua Land Surface Temperature/3-Band Emissivity Daily L3 Global 1 km SIN Grid Night V061	Skin temperature	TIR	1 km	Daily
Himawari-7	**MTSAT**	Copernicus LST version 2	Skin temperature	TIR	5 km	hourly
AIRS	**AIRS3STD**	AIRS/Aqua L3 Daily Standard Physical Retrieval (AIRS-only) 1° × 1°V006	Air/ Skin temperature	TIR	1°	Daily
AMSR2	**LPDR**	Version 3 global land parameter data record	Air temperature	PMW	25 km	Daily
MIRS	**MIRSAIMG**	MIRS Precipitation and Surface Products	Skin temperature	PMW	~27 km	Daily
ERA5	**ERA5**	ERA5 hourly data on single levels from 1979 to present	Air/ Skin/ Soil temperature	Re-analysis	0.1°	hourly
All-weather LST (Xu)	**–**	1 km seamless land surface temperature dataset of China	Skin temperature	All-weather	1 km	Daily
All-weather LST (Zhang)	**TRIMS LST-TP**	Western China Daily 1 km spatial resolution all-weather land surface temperature data set V1	Skin temperature	All-weather	1 km	Daily

methods used. Therefore, there is a need for a unified and comprehensive validation using consistent validation datasets to deliver coherent conclusions and comparable metrics for different products and variables to support the appropriate selection of data for various applications.

Representativeness of in-situ data at the satellite pixel scale is a significant issue when validating gridded datasets (Li et al. 2013b). Previous studies have investigated the issue of spatial heterogeneity in near-surface temperature data. For instance, Cao et al. (2021) found that air temperature exhibited strong spatial heterogeneity that varies with time, while Xu et al. (2019) analyzed the spatial heterogeneity of LST and found that it was generally stronger during the daytime than at night. However, the specific characteristics of different near-surface temperatures in terms of spatial heterogeneity have not been comprehensively investigated.

Furthermore, some remote sensing sensors have limited capability to obtain data in the presence of clouds. This led to barriers in applications that relied on all-weather data due to the significant differences between clear-sky data and cloud-covered data. As mentioned by Chakraborty et al. (2020), clear-sky LSTs might not have been representative of climatological mean states. Thus, it was necessary to investigate the differences between clear-sky and cloudy-sky temperatures. Previous studies by Østby et al. (2014), Ermida et al. (2019), and Liao et al. (2022) analyzed the difference in LST under various cloudy conditions. However, the all-weather LST and PMW LST data products they used contained uncertainties. Therefore, to better understand the clear-sky bias for different near-surface temperature variables, the field measurement data could be used as the optimal proxy.

The Heihe River Basin (HRB) is an ideal experimental area for studying land surface processes (Liu et al. 2018b). The Heihe Integrated Observatory Network collected multiple temperature variables and other hydrometeorological variables, providing a unique opportunity to validate multiple temperature variables, investigate their relationships, and analyze their spatial heterogeneity and clear-sky bias. Moreover, the network included multiple sites with short distances and different landscapes, making it possible to aggregate in-situ data for investigating the spatial heterogeneity of various near-surface temperature variables.

This study used in-situ data collected at HRB to evaluate various near-surface temperature products and analyzed the spatial heterogeneity and clear-sky bias for different near-surface temperature variables. The goal was to provide coherent conclusions and comparable metrics of quality assessment. The structure of this paper is as follows: Sections 2 and 3 introduce the data and validation methods. Section 4 presents the results, and finally, Section 5 provides the conclusions.

2. Gridded datasets and in-situ measurements

Nine gridded datasets for various variables such as air temperature, LST, and soil temperature, were collected for this research and their key characteristics are presented in Table 1. All available data from January 1 to December 31, 2014, were collected. In addition to the gridded data, the in-situ measurements, and auxiliary data on land cover (LC) type and elevation were collected for validation and analysis.

2.1. Gridded datasets

2.1.1. Thermal infrared temperature products

MODIS official LST products include two separate data suites. The MXD11 and MXD21 LST data are generated using the split-window technique (Wan 2014; Wan and Dozier 1996), and ASTER temperature/emissivity separation (TES) techniques (Hulley et al. 2014), respectively. The quality flag of MXD11 data is determined by cloud effects, average emissivity, and LST error; while that of MXD21 data is determined by missing data and calibration conditions, cloud conditions, atmospheric opacity, LST accuracy, emissivity, min–max difference for thermal bands and algorithm iteration rate (Hulley et al. 2016; Tan et al. 2021).

The Copernicus LST version 2 datasets include LST data from multiple sensors onboard different geostationary (GEO) satellites, including the Meteosat Second Generation (MSG), Geostationary Operational Environmental Satellite (GOES), and Multifunction Transport Satellite (MTSAT). These LST data are estimated from the Top-of-Atmosphere (TOA) brightness temperature (BT) from the infrared spectral channels of these GEO satellites, together with the albedo, vegetation cover, and soil moisture (Freitas et al. 2013). Himawari-7 data, which covers HRB, was used in this study.

The Atmospheric Infrared Sounder (AIRS) is a grating spectrometer ($R = 1200$) onboard Aqua that consists of 2378 infrared channels and four visible/near-infrared channels. The AIRS retrieval system is designed to obtain highly accurate atmospheric temperature and moisture profiles, as well as a variety of additional earth/atmosphere products. The fundamental principle of this system is to generate clear column radiances for each channel (Susskind et al. 2014). Its products

Table 2
Key information for the station observation used in this study. The symbol '@' denotes a specific condition. For instance, if an instrument is labeled with '±0.2℃ @20℃', it means that the stated accuracy of the instrument is ± 0.2 °C only when the environmental temperature is 20 °C.

Station	Arou	Shenshawo Sandy Desert	Dashalong	Zhangye Wetland	Bajitan Gobi	Huazhaizi Desert Steppe	Daman
Short Name	AR	SSW	DSL	ZY	BJT	HZZ	DM
Landscape (Liu et al. 2018a)	subalpine meadow	sandy desert	marsh alpine meadow	reed	Reaumuria desert	Kalidium foliatum desert	maize
Longitude (°)	100.46	100.49	98.94	100.45	100.3	100.32	100.37
Latitude (°)	38.05	38.79	38.84	38.98	38.92	38.77	38.86
Elevation (m)	3033	1594	3739	1460	1562	1731	1556
MODIS LC Type	Grasslands	Barren	Grasslands	Crops	Barren	Grasslands	Crops
Sensor, manufacturer and accuracy	**Air temperature**	HMP45C, Vaisala	HMP45AC, Vaisala	HMP45C, Vaisala	HMP45AC, Vaisala	AV-14TH, Avalon	
		±0.2℃ @20℃	±0.1℃				
	Surface longwave upwelling and downward radiation	CNR4, Kipp & Zonen	CNR1, Kipp & Zonen	PSP&PIR, EPPLEY			
		Uncertainty in daily total: Pyranometer: <5 % Pyrgeometer: < 10 %	Uncertainty in daily total: Pyranometer: ±10 % Pyrgeometer: ± 10 %	±5 %			
	Soil temperature	109, CSI	109ss-L, CSI	AV-10 T, Avalon			
		−40 ℃: ±0.6 ℃ tolerance; 0 ℃: ±0.38 ℃ tolerance; 25 ℃: ±0.1 ℃ tolerance; 50 ℃: ±0.3 ℃ tolerance; 70 ℃: ±0.4 ℃ tolerance;	< ±0.2℃ over 0 to 60℃; ±0.4℃ @-35℃				

have been widely used to improve weather and drought forecasting. The AIRS/Aqua L3 Daily Standard Physical Retrieval (AIRS-only) 1°× 1° product (v006) was used in this study (Kahn et al. 2014).

2.1.2. Passive microwave temperature products

The Advanced Microwave Scanning Radiometer - Earth Observing System (AMSR-E) sensor and Advanced Microwave Scanning Radiometer 2 (AMSR2) sensor are onboard the Aqua and Global Change Observation Mission 1st-Water (GCOM-W1) satellites, respectively. The Version 3 global land parameter data record (LPDR) provides the simultaneous estimation of several land parameters by using daily BT records as the primary input to an iterative retrieval algorithm (Du et al. 2014). Daily AMSR-E and AMSR2 surface air temperature minima and maxima (~2 m height) estimations are provided. The AMSR2 air temperature corresponding to the study period was selected.

The Microwave Integrated Retrieval System (MIRS) is a 1-D variational and iterative physical inversion system (Boukabara et al. 2011). Some sounder products (JPSS_SND) is generated by using Cross-track Infrared Sounder (CrIS) and Advanced Technology Microwave Sounder (ATMS) sensor data records and intermediate products from the Joint Polar Satellite System (JPSS). The MIRS precipitation and surface products are JPSS_SND products that provide skin temperature. The data have a similar observation time as the MODIS/Aqua data, and its spatial resolution is approximately 25–30 km at the nadir, increasing to approximately 100 km at the edge of the scan.

2.1.3. Re-analysis temperature products

Re-analysis data is a combination of model forecast data and newly acquired observations to form the best new estimate using data assimilation methods (Hennermann and Berrisford 2017). The ECMWF develops several atmospheric and ocean re-analysis products (Dee et al. 2011). The ERA5 is its latest atmospheric re-analysis data, offering a global improvement based on 10 years of model and data assimilation development. The ERA5 hourly data on single levels from 1979 to the present were used in this research and provide hourly estimates for a large number of atmospheric, ocean waves, and land surface quantities (Hersbach et al. 2018). In this study, 2 m air temperature, skin temperature, and soil temperature levels 1/2/3 (soil depths: 0–7, 7–28, and 28–100 cm) were used.

2.1.4. All-weather temperature products

Xu's 1 km seamless LST dataset of China is generated by fusing MODIS/Aqua LST and AMSR-E/AMSR2 data (Xu and Cheng 2021). First, an empirical retrieval algorithm based on a look-up table (LUT) and a downscaled algorithm based on geographically weighted regression (GWR) is used to generate the AMSR-E/AMSR2 LST and 1 km downscaled AMSR-E/AMSR2 LST. The cumulative distribution function (CDF) matching method is then used to adjust the downscaled AMSR-E/AMSR2 LST to improve its accuracy and fill the MODIS LST to generate the completely filled MODIS LST. Finally, the multi-scale Kalman filter (MKF) approach is used to fuse the AMSR-E/AMSR2 LST, and the completely filled MODIS LST to generate a 1 km seamless LST dataset.

Zhang's Western China daily 1 km spatial resolution all-weather LST dataset V1 is generated using a method based on temporal component decomposition (Zhang et al. 2019). In this method, LST is decomposed into three temporal components: the annual temperature cycle component (ATC), diurnal temperature cycle component (ΔDTC), and weather temperature component (WTC). Its main input data include MODIS/Aqua LST, AMSR-E/AMSR2 data, and LST from the China Meteorological Administration Land Data Assimilation System (CLDAS) and Global Land Data Assimilation System (GLDAS). In this method, the 1-km ATC is derived from discontinuous MODIS/Aqua and AMSR-E/AMSR2 LST, and the 1-km ΔDTC is derived from CLDAS and GLDAS LST. Then, the 1-km WTC is derived from the continuous daily AMSR-E/AMSR2 LST, and the daily 1 km all-weather LST is obtained by summing the ATC, ΔDTC, and WTC.

2.1.5. Auxiliary data

The MODIS level-3 standard product, MCD12Q1, was used as auxiliary data to identify the LC type for each station. This product combines observations from the MODIS sensors on the Aqua and Terra satellites and provides five LC-type datasets with different classification schemes. The study specifically used the LC data generated using the widely used International Geosphere-Biosphere Program (IGBP) system.

The Shuttle Radar Topography Mission (SRTM) dataset was employed as auxiliary data to analyze the variation in elevation within the footprint of coarse spatial resolution data. The SRTM is a global elevation dataset that was collected using radar equipment onboard the space shuttle Endeavour in February 2000. We downloaded the data

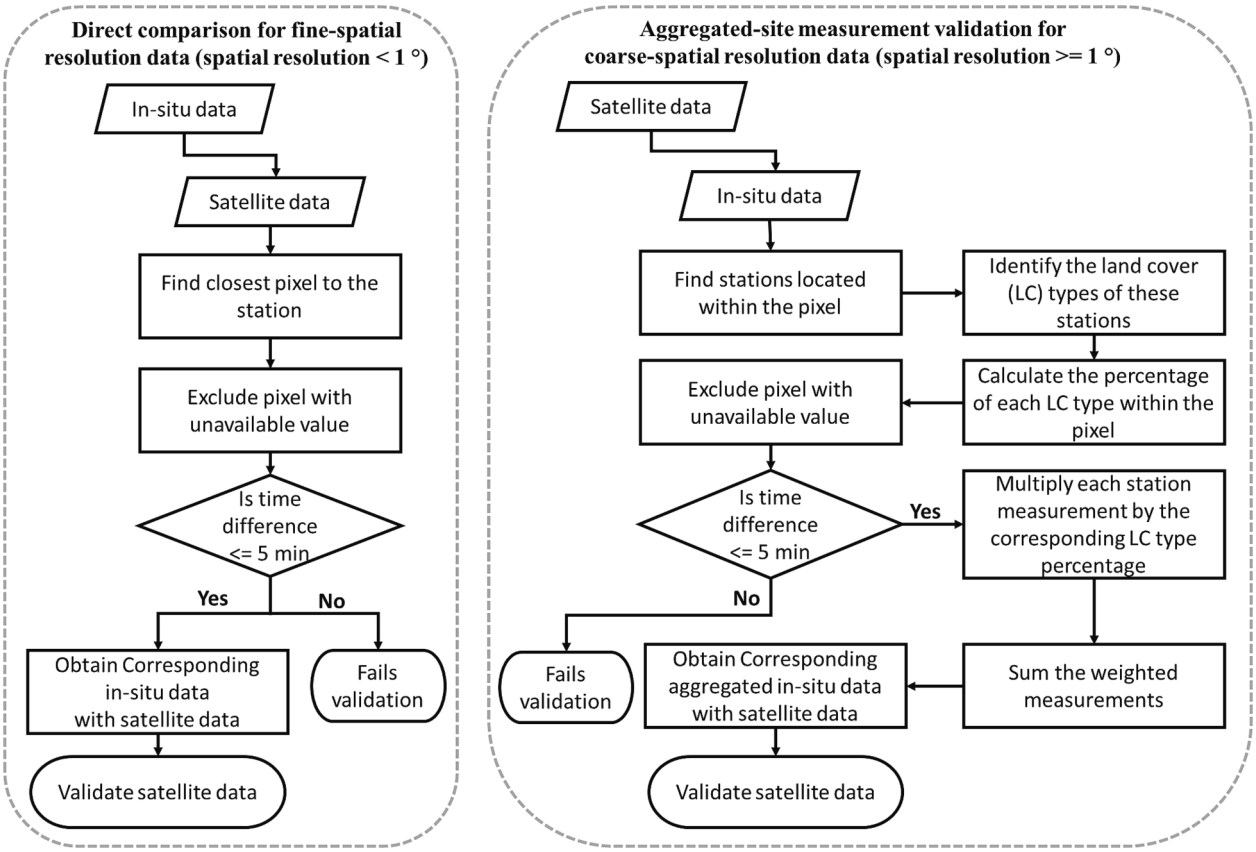

Fig. 1. The flow chart of validating gridded near surface temperature products.

from https://srtm.csi.cgiar.org/srtmdata/, and it had a spatial resolution of approximately 30 m.

2.2. In-situ measurements

2.2.1. Measurement network and site information

A hydrometeorological observation network dataset is generated by the Heihe Watershed Allied Telemetry Experimental Research (HiWATER) project (Li et al. 2013a; Liu et al. 2018a). The dataset includes multiple hydrometeorological variables, including different variables of near-surface temperature, which can help validate multiple temperature variables, analyze their spatial heterogeneity and clear-sky bias, and explore their relationships. In addition, these measurements are from multiple sites with close locations and different LC types, providing an opportunity to generate new in-situ data that match the spatial resolution of the satellite data and help explore the spatial heterogeneity issue. The stations of DSL and AR belong to the upstream of HRB, and other stations belong to the midstream of HRB (Che et al. 2019). The near-surface air temperature, near 2 m air temperature, 0 cm soil temperature, near soil temperature level 1/2/3 data, surface longwave upwelling, and downward radiation from multiple sites with different LC types in close proximity were used in this study. Key information for these sites is provided in Table 2.

2.2.2. Correlation among various temperature variables

The relationships among different variables of near-surface temperatures in the vegetated and non-vegetated areas during the daytime and nighttime were investigated by using in-situ measurements.

Adjacent near-surface soil temperatures had a strong relationship (r (correlation coefficient) > 0.95). There was a time lag between soil and air temperatures due to the relatively large heat capacity of the ground. Near soil temperature level 1 was relatively closer to 2 m air temperature than the soil temperatures at greater depths, so near soil temperature level 1 and 2 m air temperature had a relatively small time lag and high correlation ($r > 0.91$). Soil temperature was usually considered to be the result of air temperature in the previous few days (Zheng et al. 1993); therefore, although the correlation between near-surface soil temperature and the air temperature was relatively high, it was still lower than that between neighboring soil temperatures.

In most cases, the correlations in the non-vegetated areas were stronger than those in the vegetated areas, but the correlations between near soil temperature levels 1 and 2 and between nighttime 2 m air temperature and nighttime LST were stronger in the vegetated area than in the non-vegetated area. Nighttime near-surface temperatures had stronger correlations than daytime near-surface temperatures.

Interestingly, the correlation between LST and 0 cm soil temperature was also high ($r > 0.92$), but it differed between non-vegetated and vegetated areas. When vegetation was present, LST, calculated from upward and downward longwave radiance, was the result for both vegetation canopy and soil. Therefore, in the desert, the LST was similar to the 0 cm soil temperature, but not so in the meadow, and maize landscapes. Their biases over vegetated sites ranged from −5.22 K to −2.06 K, and the negative bias indicated that the LST and the canopy temperature were lower than the 0 cm soil temperature in vegetated areas.

3. Methods

3.1. Direct comparison

The selected in-situ measurements are those close to the pixel's observation time, with a maximum time difference of 5 min. Fig. 1 provides an overview of the direct comparison method. The air and soil temperatures are directly obtained from field measurements. To obtain

Table 3
The percentages of valid pixels and overall root mean square errors (RMSEs) for the datasets assessed in this study. The available pixel percentages: the hourly Himawari-7 and ERA5 data that corresponded to the MODIS/Aqua overpass time was assessed; for MODIS and Himawari-7 data, the numbers outside and inside the brackets represented the available and high-quality pixel percentages, respectively. The overall RMSEs: for MODIS and Himawari-7 data, the numbers outside of brackets represented the overall RMSEs, while the numbers before/ after the slash in the brackets represented the RMSEs of high-quality data/ low-quality data; for coarse-spatial resolution data (AIRS, MIRS, AMSR2), the numbers outside/ inside of brackets represented validation results using aggregated-site in-situ measurements/ by direct comparison; for all-weather, passive microwave (PMW) and re-analysis data, the numbers outside the brackets represented the overall RMSEs, while the numbers before/ after the slash in the brackets represented the RMSEs of clear-sky data/ cloudy-sky data.

Variables	Type	Data	Available Pixel Percentage-Day (%)	Available Pixel Percentage-Night (%)	RMSE-Day	RMSE-Night
Skin temperature	TIR	**MOD11A1**	57.4 (42.9)	54.8 (37.9)	4.15 K (3.57 K/5.57 K)	4.03 K (2.78 K/ 5.95 K)
	TIR	**MOD21A1**	54.3 (38.8)	43.1 (26.5)	4.61 K (4.12 K/5.67 K)	2.51 K (1.55 K/3.55 K)
	TIR	**MYD11A1**	51.4 (38.1)	58.3 (43.0)	4.68 K (4.09 K/ 6.10 K)	3.24 K (2.48 K/4.77 K)
	TIR	**MYD21A1**	50.8 (35.7)	45.5 (30.1)	4.36 K (3.86 K/ 5.39 K)	1.90 K (1.43 K/ 2.60 K)
	TIR	**Himawari-7**	44.4 (38.1)	56.3 (53.2)	6.64 K (6.59 K/ 7.06 K)	3.54 K (3.48 K/ 4.98 K)
	TIR	**AIRS**	74.2	81.0	6.35 K (10.25 K)	4.58 K (6.78 K)
	PMW	**MIRS**	94.9	94.7	5.51 K (7.85 K) (5.49 K/ 5.52 K)	7.44 K (7.67 K) (8.34 K/ 6.89 K)
	Re-analysis	**ERA5**	100	100	8.79 K (9.88 K/ 7.51 K)	6.04 K (5.9 K)
	All-weather	**All-weather LST (Xu)**	100	100	4.72 K (4.28 K/ 5.16 K)	3.68 K (2.45 K/ 4.60 K)
	All-weather	**All-weather LST (Zhang)**	100	100	4.81 K (4.29 K/5.33 K)	3.76 K (2.68 K/ 4.60 K)
Air temperature	TIR	**AIRS**	84.1	83.1	3.53 K (6.90 K)	4.04 K (6.61 K)
	PMW	**AMSR2**	32.1	32.8	2.55 K (2.57 K) (2.59 K/ 2.47 K)	1.67 K (2.39 K) (1.62 K/ 1.72 K)
	Re-analysis	**ERA5**	100	100	3.19 K (3.00 K/ 3.38 K)	4.55 K (4.06 K/ 4.94 K)
Soil temperature	Re-analysis	**ERA5 (0–7 cm)**	100	100	5.73 K (6.44 K/ 4.90 K)	5.02 K (5.23 K/ 4.84 K)
	Re-analysis	**ERA5 (7–28 cm)**	100	100	3.37 K (3.31 K/ 3.43 K)	3.92 K (4.10 K/ 3.76 K)
	Re-analysis	**ERA5 (28–100 cm)**	100	100	3.62 K (3.73 K/ 3.51 K)	3.56 K (3.68 K/ 3.46 K)

LST, the surface longwave upwelling and downward radiation are input to the Stefan-Boltzmann (Equation 1):

$$T_s = \left[\frac{F\uparrow - (1-\varepsilon_b)F\downarrow}{\sigma\varepsilon_b}\right]^{1/4} \quad (1)$$

where T_s is the LST, $F\uparrow$ and $F\downarrow$are the surface longwave upwelling and downward radiation, ε_b is the surface broadband emissivity (BBE), and σ is the Stefan-Boltzmann constant (5.67×10^{-8} $Wm^{-2}K^{-4}$). In this study, ε_b is estimated from the ASTER GED product (Hulley and Hook 2009) using the following linear equation, according to Cheng et al. (2013):

$$\varepsilon_b = 0.197 + 0.025\varepsilon_{10} + 0.057\varepsilon_{11} + 0.237\varepsilon_{12} + 0.333\varepsilon_{13} + 0.146\varepsilon_{14} \quad (2)$$

where ε_{10}-ε_{14} are the surface narrowband emissivities of ASTER bands 10–14, respectively.

3.2. Aggregated-site measurement validation for coarse-spatial resolution data

An aggregated-site validation method is proposed to handle the spatial scaling issue in validating the coarse-spatial grid products (spatial resolution >= 1°), which included AMSR2, MIRS, and AIRS with spatial resolutions of 25 km, 27 km, and 1°, respectively. For grids that included multiple in-situ measurement sites, the in-situ measurements contained in the same grid are aggregated before validating their near-surface temperature products (Fig. 1).

4. Results

4.1. Data quality assessment

4.1.1. Data availability

Table 3 displays the available pixel percentages for the datasets used in this study. The TIR temperature data had numerous missing values caused by clouds, resulting in a lower available pixel percentage for MODIS, Himawari-7, and AIRS data at 52.0 %, 50.4 %, and 77.6 %, respectively. The AIRS dataset had a higher valid pixel percentage compared to others due to containing cloud-free data and data for thin cloud conditions (Evan Manning et al. 2020). The high-quality percentages for MODIS and Himawari-7 data were 36.6 % and 45.7 %, respectively, for various reasons mentioned in Section 2.1. MXD11 had higher available and high-quality pixel percentages than MXD21 data; the available pixel percentages for MXD11 and MXD21 data were 55.5 %, and 48.4 %, respectively, and the high-quality pixel percentages were 40.5 %, and 32.8 %, respectively.

PMW data theoretically had fewer missing values because of its capability of penetrating clouds. The available pixel percentage for MIRS data was 94.8 %. However, the percentage of available pixels for AMSR2 was only 32.5 % due to orbit gaps and algorithm restrictions. The orbit gaps were filled with fill values, with a percentage of 32.0 % (32.8 %) during the daytime (nighttime). The retrieval algorithm skipped pixels with the frozen ground (Freeze-thaw Earth System Data Record (Kim et al. 2017)), strong precipitation, snow cover, active rainfall, and identified radio frequency interference (RFI). In this study, frozen ground and strong precipitation occurred at 45.8 % (44.7 %) and 0.04 % (0.0 %) during daytime (nighttime).

4.1.2. Overall data accuracy

The overall RMSE is also summarized in Table 3. AIRS and ERA5 products provided both air and skin temperature. The daytime/nighttime RMSEs for AIRS and ERA5 air temperature were 3.53 K/4.04 K and 3.19 K/4.55 K, respectively and the daytime/nighttime RMSEs for AIRS and ERA5 skin temperature were 6.35 K/4.58 K and 8.79 K/6.04 K, respectively, indicating that their air temperatures were more accurate than their skin temperature. For PMW data, the daytime/nighttime RMSEs for AMSR2 air temperature and MIRS skin temperature were 2.55 K/1.67 K and 5.51 K/7.44 K, respectively, indicating that the

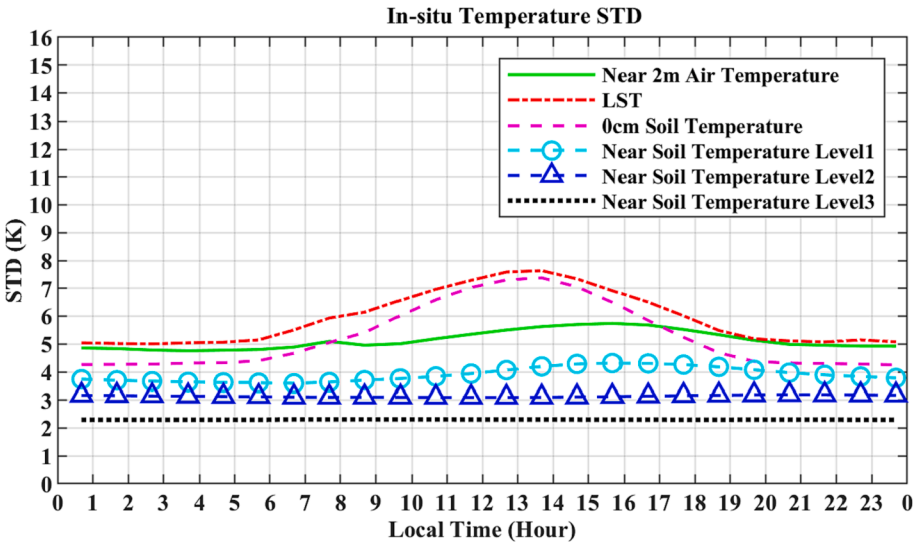

Fig. 2. Temporal variations in the spatial variability of multiple variables: the diurnal series of spatial variability (Daytime is from 7:00 to 16:00 local time, and other times are nighttime).

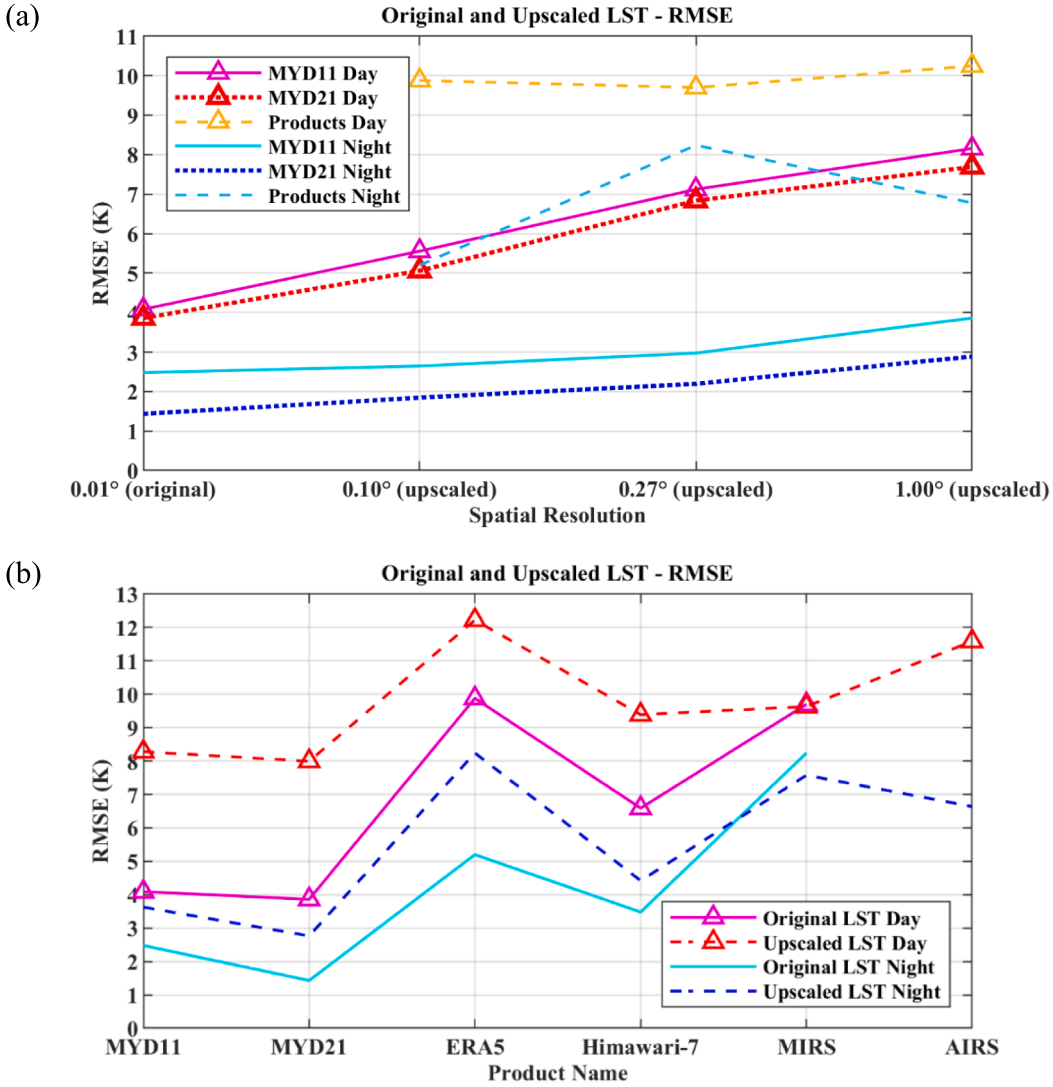

Fig. 3. The RMSEs of the original and upscaled LST compared with in-situ measurements. For (a), the products corresponding to 0.10°, 0.27°, and 1.00° spatial resolution are clear-sky ERA5, MIRS, and AIRS LST, respectively.

Table 4
The statistic of elevation within the ERA5 footprint for each ground station.

Site Name	AR	BGT	DSL	DM	HZZ	SSW	ZY
Maximum elevation (m)	3798	1634	3989	1619	2031	1636	1516
Minimum elevation (m)	2947	1501	3693	1508	1569	1513	1439
Averaged elevation (m)	3221.5	1562.8	3796.7	1557.3	1736.2	1562.0	1465.4
Station elevation (m)	3033	1562	3739	1556	1731	1594	1460
Elevation difference (m)	188.5	0.8	57.7	1.3	5.2	−32.0	5.4

accuracy of air temperature (AMSR2) was higher than that of skin temperature (MIRS).

The high-quality data had lower RMSEs than the low-quality data, with RMSE differences ranging from 1.16 K to 3.17 K for MODIS data and 0.47 K to 1.51 K for Himawari-7 data. And, it should be noted that the percentages of high-quality data in the MXD11, MXD21, and Himawari-7 products were lower than the percentage of all available data, 15.0 %, 15.7 %, and 4.7 %, respectively.

All-weather, PMW, and re-analysis products could provide clear-sky and cloudy-sky data, and their accuracies were discussed separately. The clear-sky data from the all-weather LST products exhibited lower RMSEs than the corresponding cloudy-sky data. In particular, Xu's and Zhang's all-weather LST products had lower daytime/nighttime RMSEs by 0.89 K/2.15 K and 1.04 K/1.92 K, respectively. Conversely, for PMW products, the differences in RMSE between clear-sky and cloudy-sky data were relatively small, at only 0.12 K/-0.10 K and −0.03 K/ 1.45 K for daytime/nighttime AMSR2 surface air temperature and MIRS skin temperature, respectively. On the other hand, the RMSE of clear-sky data obtained from re-analysis products was sometimes larger than that of cloudy-sky data. The differences in RMSE between the two were 2.36 K /-1.49 K, −0.38 K /-0.89 K, 1.54 K /0.40 K, −0.12 K /0.34 K, and 0.22 K /0.22 K for daytime/nighttime ERA5 skin temperature, 2 m air temperature, and soil temperature levels 1, 2 and 3 products, respectively.

In addition, the results of the direct comparison were generally consistent with previous studies on individual temperature variables. For air temperature, the average RMSEs for the AIRS, AMSR2, and ERA5 products were 6.76 K, 2.48 K, and 3.87 K, similar to 6.18 K (RMSE) (Zhang 2017), 3.50 K (RMSE) (Jones et al. 2010), and 0.88–3.07 K (MAE) (Cao et al. 2020) in previous studies. For LST, the average RMSEs for the high-quality MXD11, high-quality MXD21, high-quality Himawari-7, ERA5, and Xu's all-weather LST were 3.23 K, 2.74 K, 5.04 K, 7.42 K, 4.20 K, similar to 0.75–5.58 K (RMSE) (Duan et al. 2019), 0.33–2.20 K (RMSE) (Duan et al. 2018), 5.00 K (RMSD) (Trigo and Macedo 2015), −5.50–4.50 K (Bias) (Gleixner et al. 2020), 2.85–3.72 K (RMSE) (Xu and Cheng 2021) in previous studies; The RMSEs for Zhang's all-weather LST were 3.76–4.81 K in this study and 1.29–2.71 K (Zhang et al. 2019) in the previous study, and the differences might be due to the different validation sites used and the high spatial heterogeneity around the Heihe sites used in this study. The average RMSEs for ERA5 soil temperature levels 1/2/3 were 5.38 K, 3.65 K, and 3.59 K, and their accuracies in previous studies were 1.81–4.85 K (MAE), 1.74–4.42 K (MAE), 1.65–3.73 K (MAE) (Cao et al. 2020).

4.2. Spatial heterogeneity of near surface temperatures

The section includes three separate analyses, with Section 4.2.1 based on in situ data and Sections 4.2.2 and 4.2.3 based on gridded products.

4.2.1. Temporal variations of spatial variability

To investigate spatial variability, the standard deviation (STD) was calculated using the in-situ temperatures across all sites at the same moment as an indicator. The STD for the diurnal series was obtained by averaging the STD values for all days at the same moment and is presented in Fig. 2. The LST had the highest spatial variability, while the air and soil temperatures had the lowest spatial variability. Moreover, the daytime data showed higher spatial variability than the nighttime data. The 0 cm soil temperatures and LST had the most significant diurnal variation in spatial variability. Their spatial variability increased from 6:00 to 13:00 local time, decreased from 14:00 to 20:00 local time, and tended to be constant at other times of the day. The spatial variability of near 2 m air temperature and near soil temperature level 1 varied only slightly throughout the day. Their spatial variability slightly increased from 9:00 to 18:00 local time, slightly decreased from 18:00 to 23:00 local time and tended to be constant at other times of the day. The spatial variability near soil temperature levels 2 and 3 was approximately constant during the day.

4.2.2. Impact of spatial resolution on validating LST products

To investigate the impact of spatial heterogeneity on the validation results, MODIS LST data were upscaled to 0.10°, 0.27°, and 1.00° spatial resolutions, corresponding to ERA5, MIRS, and AIRS LST products, and then compared with field measurements. Fig. 3a shows the accuracy at various aggregated resolutions. RMSE of the actual product of the same resolution is also displayed for reference. All the values correspond to clear-sky conditions when MODIS LST products are available.

As the spatial resolution increased, the RMSE generally increased, indicating that the data validation results were subject to scale effects. For each product, the nighttime data had higher accuracy than the daytime data. For both the daytime and nighttime data, at each spatial resolution, the actual products had higher RMSEs than the upscaled MODIS data, indicating that the coarse-spatial resolution data were in fact less accurate than the aggregated MODIS data.

4.2.3. Accuracy of various LST products when aggregated to the same resolution

To exclude the effects of resolution differences in validation, the MYD11, MYD21, ERA5, Himawari-7, and MIRS products were upscaled to the coarsest resolution (AIRS) and compared with in-situ measurements (Fig. 3b).

The RMSEs of the original LST data were also provided. The majority of original LSTs had lower RMSEs than the upscaled data, suggesting that the validation results were impacted by scale effects. However, the RMSEs did not exhibit a monotonic increase with the spatial resolution, as this could be influenced by variations in data sources and retrieval algorithms.

4.2.4. The difference in elevation within the footprint of coarse spatial resolution data

The spatial resolution of satellite products, such as AMSR2, AIRS, and ERA5 data, is coarser than station data, and their elevation representation can differ from that of stations.

To investigate this issue, we analyzed the elevation difference between grid and station elevation. Using the nighttime ERA5 air temperature data as example, we extracted the SRTM elevation data within the ERA5 pixels located by stations and provided statistics of maximum elevation, minimum elevation, the averaged elevation within the ERA5 pixels. The elevation of the station, and the elevation difference between the averaged elevation and the elevation for each station were summarized in Table 4. The absolute value of elevation difference between the averaged elevation within the ERA5 pixels and the elevation of the

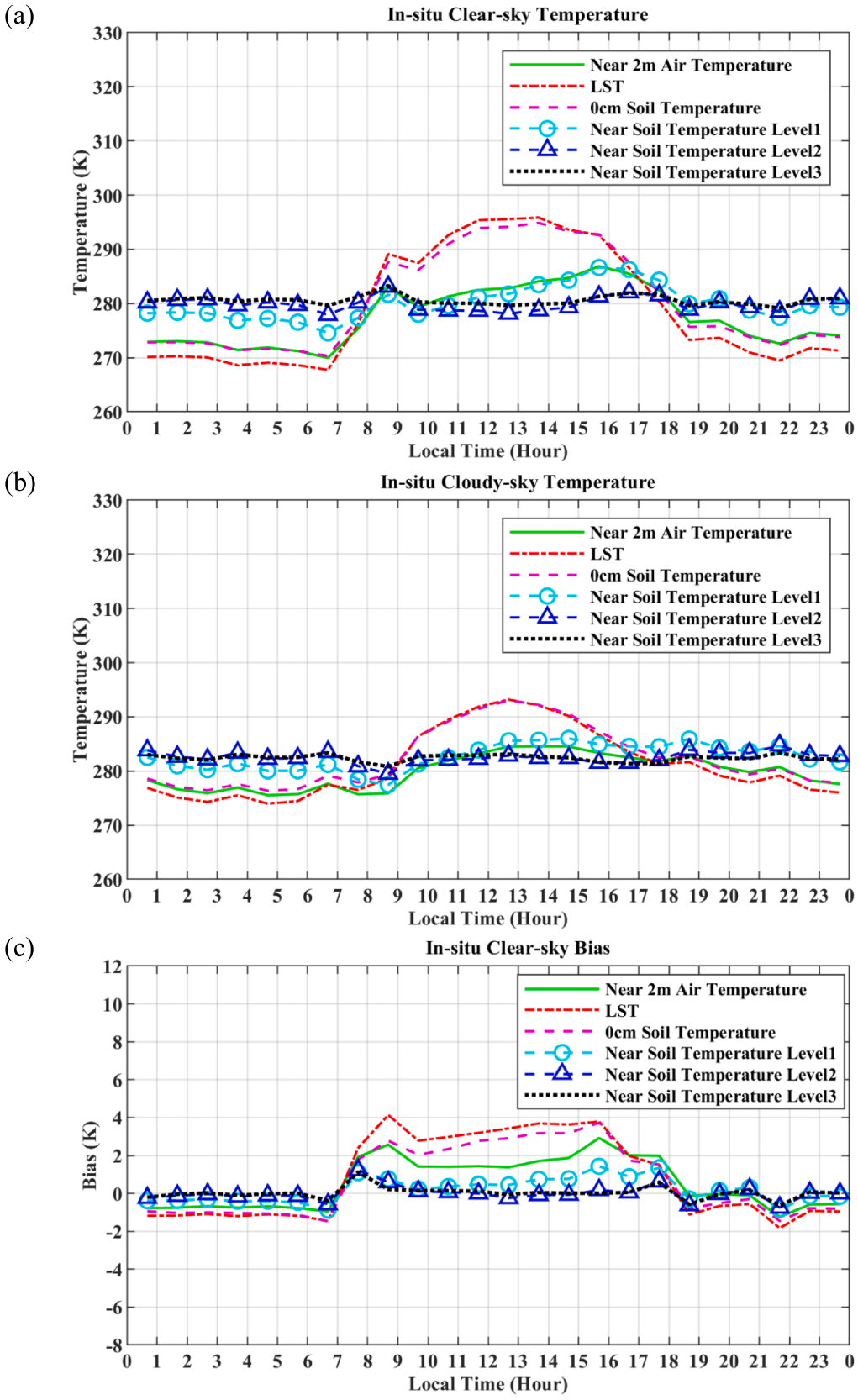

Fig. 4. Diurnal series of clear-sky temperature, cloudy-sky temperature, and clear-sky bias.

station has a range from 0.8 m to 188.5 m. According to Wang et al. (2018), the change in air temperature due to elevation difference varies from 2.4 °C/km to 8.7 °C/km in the vertical direction. Therefore, the elevation difference may cause an air temperature difference from 0.0 °C to 1.6 °C at these stations.

4.3. Clear-sky bias

Clear-sky bias was defined as the difference between the average clear-sky and all-weather LSTs, using the in-situ data in this study. This section presents the diurnal variation in clear-sky bias for near-surface temperature variables.

Fig. 4 shows the diurnal series of clear-sky temperature, cloudy-sky temperature, and clear-sky bias. In general, the variation in LST, 0 cm soil, and the air temperature was larger than the variation in soil temperatures at greater depths. Among all near-surface temperature variables, the variation in cloudy-sky data was smaller than that in clear-sky data. During the daytime, the clear-sky temperature was higher than the cloudy-sky temperatures, while the opposite was true at night. This phenomenon could be attributed to the cooling/warming effects of clouds on the land surface during daytime/nighttime, as reported by Tan et al. (2021). As a result, a positive clear-sky bias was observed during the daytime, while a negative clear-sky bias was observed at night. Moreover, the clear-sky bias for LST, 0 cm soil temperature, and air temperature exhibited the most substantial temporal variations.

5. Conclusions

This study presented a comprehensive evaluation of nine gridded datasets of various near-surface temperature variables, including air, land surface, and soil temperatures, using in-situ measurements collected at HRB. With the extensive measurements of various temperature variables at HRB, the study also investigated the spatial heterogeneity and clear-sky bias of different temperature variables.

The results indicated that the MXD21 products had high accuracy for skin temperatures but low data availability, while the gap-free all-weather LST products with comparable accuracy can be promising alternatives. Products of near-surface air temperatures generally had high accuracy. For the EAR5 soil temperature data, the data accuracy increased with the reference depth. For various temperature variables from the same products (AIRS, ERA5), the air and soil temperatures had higher accuracy than the skin temperature.

The spatial heterogeneity of air temperature and soil temperature at deep layers was low. In contrast, skin temperature and 0 cm soil temperature had stronger spatial variations. The spatial heterogeneity also varied with the time of day, with daytime temperatures usually having higher spatial variations than nighttime data. The issue of spatial heterogeneity is further complicated by the difference in elevation within the footprint of coarse spatial resolution temperature data. The lapse rate in mountainous arear was reported to display great variability depending on season and synoptic weather types (Blandford et al. 2008). Incorrect representation of the elevation signature within the data grid can lead to substantial uncertainties in gridded temperature data, sometime even results in artifact trends (Wang et al. 2018). Similarly, the difference between the station elevation and the elevation of coarse resolution product represents a significant source of error that should not be ignored. The issue is worthy further investigation in the future.

For clear-sky biases in these temperature variables, deep soil temperatures were less affected than the air temperature and skin temperature. The magnitude and sign of clear-sky bias showed strong diurnal variations, with the daytime clear-sky bias being positive and the nighttime clear-sky bias being negative.

It should be noted that conclusions obtained in this study were based on data measured at a limited number of sites in HRB, and further analysis using additional data acquired over other regions and from extra years was needed to provide an extensive quality assessment of various temperature variables. The use of spatially weighted aggregation of measurements from multiple sites within the footprint of a satellite sensor was a promising approach to explicitly account for spatial heterogeneity and reliably evaluate the quality of coarse-resolution temperature data products. However, such analysis was limited to only a few locations in this study due to the number of stations in HRB and their spatial distribution. A measurement network with dense stations and strategically designed spatial distribution was desired to fully investigate the spatial heterogeneity issue of temperature variables.

CRediT authorship contribution statement

Shuo Xu: Conceptualization, Data curation, Formal analysis, Writing – original draft, Writing – review & editing. **Dongdong Wang:** Conceptualization, Supervision, Data curation, Formal analysis, Writing – review & editing. **Shunlin Liang:** Writing – review & editing. **Yuling Liu:** Writing – review & editing. **Aolin Jia:** Writing – review & editing.

Declaration of Competing Interest

The authors declare that they have no known competing financial interests or personal relationships that could have appeared to influence the work reported in this paper.

Data availability

Data will be made available on request.

Acknowledgments

This study was supported by National Oceanic and Atmospheric Administration (NOAA) grant NA14NES4320003 (Cooperative Institute for Climate and Satellite-CICS) at the University of Maryland/ESSIC.

The authors would like to thank the Land Processes Distributed Active Archive Center, Copernicus Global Land Service, Goddard Earth Sciences Data and Information Service Center, NOAA's Comprehensive Large Array-Data Stewardship System, Copernicus Climate Change Service, National Tibetan Plateau Data Center, and the Numerical Terradynamic Simulation Group for providing the datasets.

References

Benali, A., Carvalho, A., Nunes, J., Carvalhais, N., Santos, A., 2012. Estimating air surface temperature in Portugal using MODIS LST data. Remote Sens. Environ. 124, 108–121.

Blandford, T.R., Humes, K.S., Harshburger, B.J., Moore, B.C., Walden, V.P., Ye, H., 2008. Seasonal and Synoptic Variations in Near-Surface Air Temperature Lapse Rates in a Mountainous Basin. J. Appl. Meteorol. Climatol. 47, 249–261.

Boukabara, S.-A., Garrett, K., Chen, W., Iturbide-Sanchez, F., Grassotti, C., Kongoli, C., Chen, R., Liu, Q., Yan, B., Weng, F., 2011. MiRS: An all-weather 1DVAR satellite data assimilation and retrieval system. IEEE Trans. Geosci. Remote Sens. 49, 3249–3272.

Cao, B., Gruber, S., Zheng, D., Li, X., 2020. The ERA5-Land soil temperature bias in permafrost regions. Cryosphere 14, 2581–2595.

Cao, J., Zhou, W., Zheng, Z., Ren, T., Wang, W., 2021. Within-city spatial and temporal heterogeneity of air temperature and its relationship with land surface temperature. Landsc. Urban Plan. 206, 103979.

Chakraborty, T., Hsu, A., Manya, D., Sheriff, G., 2020. A spatially explicit surface urban heat island database for the United States: Characterization, uncertainties, and possible applications. ISPRS J. Photogramm. Remote Sens. 168, 74–88.

Che, T., Li, X., Liu, S., Li, H., Xu, Z., Tan, J., Zhang, Y., Ren, Z., Xiao, L., Deng, J., Jin, R., Ma, M., Wang, J., Yang, X., 2019. Integrated hydrometeorological, snow and frozen-ground observations in the alpine region of the Heihe River Basin. China. *Earth Syst. Sci. Data* 11, 1483–1499.

Cheng, J., Liang, S., Yao, Y., Zhang, X., 2013. Estimating the Optimal Broadband Emissivity Spectral Range for Calculating Surface Longwave Net Radiation. IEEE Geosci. Remote Sens. Lett. 10, 401–405.

Dee, D.P., Uppala, S.M., Simmons, A.J., Berrisford, P., Poli, P., Kobayashi, S., Andrae, U., Balmaseda, M., Balsamo Bauer, d.P., G., 2011. The ERA-Interim reanalysis: Configuration and performance of the data assimilation system. Q. J. R. Meteorolog. Soc. 137, 553–597.

Du, J., Kimball, J.S., Jones, L.A., 2014. Satellite microwave retrieval of total precipitable water vapor and surface air temperature over land from AMSR2. IEEE Trans. Geosci. Remote Sens. 53, 2520–2531.

Duan, S.-B., Li, Z.-L., Wu, H., Leng, P., Gao, M., Wang, C., 2018. Radiance-based validation of land surface temperature products derived from Collection 6 MODIS thermal infrared data. Int. J. Appl. Earth Obs. Geoinf. 70, 84–92.
Duan, S.-B., Li, Z.-L., Li, H., Göttsche, F.-M., Wu, H., Zhao, W., Leng, P., Zhang, X., Coll, C., 2019. Validation of Collection 6 MODIS land surface temperature product using in situ measurements. Remote Sens. Environ. 225, 16–29.
Ermida, S.L., Trigo, I.F., DaCamara, C.C., Jiménez, C., Prigent, C., 2019. Quantifying the Clear-Sky Bias of Satellite Land Surface Temperature Using Microwave-Based Estimates. J. Geophys. Res. Atmos. 124, 844–857.
Evan Manning, J., Larrabee Strow, U., Teixeira, J., Leader, J.A.T., Fetzer, E.J., Yue, Q., Thrastarson, H.T., 2020. AIRS-Team Retrieval For Core Products and Geophysical Parameters: Versions 6 and 7 Level 2. *Jet Propulsion*.
Freitas, S.C., Trigo, I.F., Macedo, J., Barroso, C., Silva, R., Perdigão, R., 2013. Land surface temperature from multiple geostationary satellites. Int. J. Remote Sens. 34, 3051–3068.
Gleixner, S., Demissie, T., Diro, G.T., 2020. Did ERA5 Improve Temperature and Precipitation Reanalysis over East Africa? Atmos. 11, 996.
Hennermann, K., Berrisford, P., 2017. ERA5 data documentation. *Copernicus knowledge base*.
Hersbach, H., Bell, B., Berrisford, P., Biavati, G., Horányi, A., Muñoz Sabater, J., Nicolas, J., Peubey, C., Radu, R., Rozum, I., 2018. ERA5 hourly data on single levels from 1979 to present. *Copernicus Climate Change Service (C3S) Climate Data Store (CDS), 10*.
Hu, Q., Feng, S., 2004. A role of the soil enthalpy in land memory. J. Clim. 17, 3633–3643.
Hulley, G., Veraverbeke, S., Hook, S., 2014. Thermal-based techniques for land cover change detection using a new dynamic MODIS multispectral emissivity product (MOD21). Remote Sens. Environ. 140, 755–765.
Hulley, G., Freepartner, R., Malakar, N., Sarkar, S., 2016. Moderate Resolution Imaging Spectroradiometer (MODIS) Land Surface Temperature and Emissivity Product (MxD21) User Guide. Washington, DC, USA, NASA.
Hulley, G.C., Hook, S.J., 2009. The North American ASTER Land Surface Emissivity Database (NAALSED) Version 2.0. Remote Sens. Environ. 113, 1967–1975.
Jia, A., Liang, S., Wang, D., Jiang, B., Zhang, X., 2020. Air pollution slows down surface warming over the Tibetan Plateau. Atmos. Chem. Phys. 20, 881–899.
Jia, A., Liang, S., Wang, D., Ma, L., Wang, Z., Xu, S., 2023. Global hourly, 5 km, all-sky land surface temperature data from 2011 to 2021 based on integrating geostationary and polar-orbiting satellite data. Earth Syst. Sci. Data 15, 869–895.
Jones, L.A., Ferguson, C.R., Kimball, J.S., Zhang, K., Chan, S.T.K., McDonald, K.C., Njoku, E.G., Wood, E.F., 2010. Satellite Microwave Remote Sensing of Daily Land Surface Air Temperature Minima and Maxima From AMSR-E. IEEE J. Sel. Top. Appl. Earth Obs. Remote Sens. 3, 111–123.
Kahn, B., Irion, F., Dang, V., Manning, E., Nasiri, S., Naud, C., Blaisdell, J., Schreier, M., Yue, Q., Bowman, K., 2014. The atmospheric infrared sounder version 6 cloud products. Atmos. Chem. Phys. 14, 399–426.
Kim, Y., Kimball, J.S., Glassy, J., Du, J., 2017. An extended global Earth system data record on daily landscape freeze-thaw status determined from satellite passive microwave remote sensing. Earth Syst. Sci. Data 9, 133–147.
Li, X., Cheng, G., Liu, S., Xiao, Q., Ma, M., Jin, R., Che, T., Liu, Q., Wang, W., Qi, Y., 2013a. Heihe watershed allied telemetry experimental research (HiWATER): Scientific objectives and experimental design. Bull. Am. Meteorol. Soc. 94, 1145–1160.
Li, Z.-L., Tang, B.-H., Wu, H., Ren, H., Yan, G., Wan, Z., Trigo, I.F., Sobrino, J.A., 2013b. Satellite-derived land surface temperature: Current status and perspectives. Remote Sens. Environ. 131, 14–37.
Liao, Y., Shen, X., Zhou, J., Ma, J., Zhang, X., Tang, W., Chen, Y., Ding, L., Wang, Z., 2022. Surface urban heat island detected by all-weather satellite land surface temperature. Sci. Total Environ. 811, 151405.
Liu, S., Li, X., Xu, Z., Che, T., Xiao, Q., Ma, M., Liu, Q., Jin, R., Guo, J., Wang, L., 2018a. The Heihe Integrated Observatory Network: A basin-scale land surface processes observatory in China. Vadose Zone J. 17.
Liu, S., Li, X., Xu, Z., Che, T., Xiao, Q., Ma, M., Liu, Q., Jin, R., Guo, J., Wang, L., Wang, W., Qi, Y., Li, H., Xu, T., Ran, Y., Hu, X., Shi, S., Zhu, Z., Tan, J., Zhang, Y., Ren, Z., 2018b. The Heihe Integrated Observatory Network: A Basin-Scale Land Surface Processes Observatory in China. Vadose Zone J. 17, 180072.
Muro, J., Strauch, A., Heinemann, S., Steinbach, S., Thonfeld, F., Waske, B., Diekkrüger, B., 2018. Land surface temperature trends as indicator of land use changes in wetlands. Int. J. Appl. Earth Obs. Geoinf. 70, 62–71.
Nieto, H., Sandholt, I., Aguado, I., Chuvieco, E., Stisen, S., 2011. Air temperature estimation with MSG-SEVIRI data: Calibration and validation of the TVX algorithm for the Iberian Peninsula. Remote Sens. Environ. 115, 107–116.
Østby, T.I., Schuler, T.V., Westermann, S., 2014. Severe cloud contamination of MODIS Land Surface Temperatures over an Arctic ice cap, Svalbard. Remote Sens. Environ. 142, 95–102.
Sobrino, J.A., Julien, Y., Jiménez-Muñoz, J.-C., Skokovic, D., Sòria, G., 2020. Near real-time estimation of Sea and Land surface temperature for MSG SEVIRI sensors. Int. J. Appl. Earth Obs. Geoinf. 89, 102096.
Susskind, J., Blaisdell, J.M., Iredell, L., 2014. Improved methodology for surface and atmospheric soundings, error estimates, and quality control procedures: the atmospheric infrared sounder science team version-6 retrieval algorithm. J. Appl. Remote Sens. 8, 084994.
Tan, J., Che, T., Wang, J., Liang, J., Zhang, Y., Ren, Z., 2021. Reconstruction of the Daily MODIS Land Surface Temperature Product Using the Two-Step Improved Similar Pixels Method. Remote Sens. (Basel) 13, 1671.
Trigo, I., Macedo, J., 2015. Gio global land component—Lot I "Operation of the global land component". *Framework service contract*.
Vancutsem, C., Ceccato, P., Dinku, T., Connor, S.J., 2010. Evaluation of MODIS land surface temperature data to estimate air temperature in different ecosystems over Africa. Remote Sens. Environ. 114, 449–465.
Wan, Z., 2014. New refinements and validation of the collection-6 MODIS land-surface temperature/emissivity product. Remote Sens. Environ. 140, 36–45.
Wan, Z., Dozier, J., 1996. A generalized split-window algorithm for retrieving land-surface temperature from space. IEEE Trans. Geosci. Remote Sens. 34, 892–905.
Wang, T., Sun, F., Ge, Q., Kleidon, A., Liu, W., 2018. The Effect of Elevation Bias in Interpolated Air Temperature Data Sets on Surface Warming in China During 1951–2015. J. Geophys. Res. Atmos. 123, 2141–2151.
Xu, S., Cheng, J., 2021. A new land surface temperature fusion strategy based on cumulative distribution function matching and multiresolution Kalman filtering. Remote Sens. Environ. 254, 112256.
Xu, S., Cheng, J., Zhang, Q., 2019. Reconstructing all-weather land surface temperature using the bayesian maximum entropy method over the Tibetan plateau and Heihe river basin. IEEE J. Sel. Top. Appl. Earth Obs. Remote Sens. 12, 3307–3316.
Xu, S., Cheng, J., Zhang, Q., 2021. A Random Forest-Based Data Fusion Method for Obtaining All-Weather Land Surface Temperature with High Spatial Resolution. Remote Sens. (Basel) 13, 2211.
Yang, S., Li, R., Wu, T., Hu, G., Xiao, Y., Du, Y., Zhu, X., Ni, J., Ma, J., Zhang, Y., Shi, J., Qiao, Y., 2020. Evaluation of reanalysis soil temperature and soil moisture products in permafrost regions on the Qinghai-Tibetan Plateau. Geoderma 377, 114583.
Zhang, H., Immerzeel, W.W., Zhang, F., de Kok, R.J., Gorrie, S.J., Ye, M., 2021. Creating 1-km long-term (1980–2014) daily average air temperatures over the Tibetan Plateau by integrating eight types of reanalysis and land data assimilation products downscaled with MODIS-estimated temperature lapse rates based on machine learning. Int. J. Appl. Earth Obs. Geoinf. 97, 102295.
Zhang, X., Zhou, J., Göttsche, F.-M., Zhan, W., Liu, S., Cao, R., 2019. A method based on temporal component decomposition for estimating 1-km all-weather land surface temperature by merging satellite thermal infrared and passive microwave observations. IEEE Trans. Geosci. Remote Sens. 57, 4670–4691.
Zhang, H., 2017. Estimation of daily average near-surface air temperature using MODIS and AIRS data. In, *2017 2nd International Conference on Frontiers of Sensors Technologies (ICFST)* (pp. 377-381).
Zheng, D., Hunt Jr, E.R., Running, S.W., 1993. A daily soil temperature model based on air temperature and precipitation for continental applications. Climate Res. 2, 183–191.